Scalar product for the radiation of resonant modes

Maria Paszkiewicz-Idzik [1,2,*] Lukas Rebholz [2,*] Carsten Rockstuhl [3,2] and Ivan Fernandez-Corbaton [3,†]
[1]*Scientific Computing Center, Karlsruhe Institute of Technology, Kaiserstrasse 12, D-76131 Karlsruhe, Germany*
[2]*Institute of Theoretical Solid-State Physics, Karlsruhe Institute of Technology, Kaiserstrasse 12, D-76131 Karlsruhe, Germany*
[3]*Institute of Nanotechnology, Karlsruhe Institute of Technology, Kaiserstrasse 12, D-76131 Karlsruhe, Germany*

(Received 20 March 2025; accepted 24 June 2025; published 16 July 2025)

We introduce the conformally invariant scalar product, originally devised for radiation fields, to the study of the modes of optical resonators. This scalar product allows one to normalize and compare resonant modes using their corresponding radiation fields. Such fields are polychromatic fields free of divergences, which are determined from the complex frequencies and the modal fields on the surface of the resonator. The scalar product is expressed as surface integrals involving the modal fields, multiplied by closed-form factors incorporating the complex frequencies. In a practical application, we study the modes of disk-shaped whispering gallery resonators and show that the proposed scalar product accurately predicts the geometry-dependent anticrossings between modes.

DOI: 10.1103/1rhp-ts2q

I. INTRODUCTION

Optical resonators allow us to control and enhance light-matter interactions [1]. They offer strong optical confinement, which can reduce the size of optical instruments and decrease optical loss [2]. Resonant recirculation of an input signal increases the field intensity, which finds applications in lasers and photovoltaics [1–3]. The implementation of optical resonators differs in form, materials, and principle of operation. Among the many kinds of optical resonators, the ones hosting whispering gallery modes (WGMs) are particularly attractive for many applications due to their high quality factor and unique spectral properties, such as tunability, narrow linewidth, and high stability [2,4,5].

The physics of resonators can be conveniently studied through their resonant modes [6], which are the natural damped resonances of the system. Such modes are also known as quasi-normal modes, leaky modes, electromagnetic eigenmodes, or simply, modes. In particular, resonant modes are being used for the study and engineering of light-matter interactions [7–22]. For example, the fields scattered by the resonator upon a given illumination may be expanded to a good approximation as a linear combination of a few modal fields, at least in limited frequency ranges [23,24]. The general question of orthogonality and completeness of the modal fields outside the resonator is particularly relevant for such applications [25]. Such a question is complicated by the divergence of time-harmonic modal fields as $|\mathbf{r}| \to \infty$, albeit, in principle, such divergence can be mitigated by causality [12,26]. In this context, a crucial question is *which scalar product to use for normalization and projections.* These questions have received considerable attention in recent times. Reference [8] contains a comprehensive review of the properties and suitability of several different approaches [16,27,28].

For radiated fields, there is a scalar product with many desirable properties [29]. For example, the square of the norm induced by such scalar product $\langle f|f\rangle$ gives the number of photons of the field [30]. Also, the values of fundamental quantities in the field, such as energy or momentum, can be computed as "sandwiches" $\langle f|\mathrm{G}|f\rangle$, where G is the operator representing the particular fundamental quantity ([31], Chap. 3,§9). For example, using the energy operator H, the value of $\langle f|\mathrm{H}|f\rangle$ can be shown to be identical to the typical integral giving the energy of the field. Such scalar product has the unique property of being invariant upon any conformal transformation [29]. That is, the scalar product between transformed fields is equal to the scalar product between the original fields. Since the conformal group is the largest group of invariance of Maxwell's equations [32], the conformal invariance of the scalar product is a very strong argument in favor of its use. For example, it is precisely those invariance properties that underpin the consistent frame-independent definition of projective measurements in electromagnetism ([33], Sec. III). The uses of this scalar product in light-matter interactions have been recently reviewed [34].

Here, we introduce the use of the conformally invariant scalar product for radiation fields in the study of optical resonators. We start by deriving a polychromatic radiation field free of divergences from the field profile and the complex frequency of a given electromagnetic eigenmode of a three-dimensional (3D) structure. Then, a cross-energy expression between the radiations of any two given eigenmodes, $\langle f|\mathrm{H}|g\rangle$, is identified as a suitable scalar product. The computation of

*These authors contributed equally to this work.
†Contact author: ivan.fernandez-corbaton@kit.edu

$\langle f|\mathrm{H}|g\rangle$ consists of integrals of simple functions of the modal fields at the surface of the resonator and closed-form factors involving the complex modal frequencies [see Eq. (13)]. In contrast with several existing expressions, such as Ref. [16], Eq. (4); Ref. [27], Eq. (22); or Ref. [8], Eq. (20), Eq. (13) does not involve the material parameters of the resonator, frequency derivatives thereof, or the exponentially growing fields with complex wave number. Boundary element methods such as those described in Refs. [35,36] are perfectly suited for the computation of the cross-energy scalar product.

We show that the cross-energy scalar product produces physically consistent results, by means of a first exemplary application. We study the modes of a WGM disk resonator as the thickness of the disk changes [37]. We observe that the absolute value of $\langle f|\mathrm{H}|g\rangle$ between two normalized modes is zero in particular when the real frequencies of that particular pair of modes cross. In sharp contrast, for anticrossing modes, the same quantity shows a prominent peak that grows as the real frequencies of that particular pair of modes get close to each other. The position of the peak coincides with the thickness for which the two modes anticross, and for which the modal overlap inside the resonator is maximized. The increasing nonorthogonality implies a decreasing distinguishability of the modes in the far field.

The rest of the article is organized as follows. In Sec. II, we obtain the field radiated by a given leaky mode by using the Mittag-Leffler theorem ([38], p. 515). The resulting polychromatic field is free of divergences. We insert these fields into a recent [39] surface integral expression for $\langle f|\mathrm{H}|g\rangle$, and derive the corresponding expression for radiation fields of resonant modes of 3D structures, which we call the cross-energy scalar product. In Sec. III, we apply the cross-energy scalar product to the resonant modes of a disk-shaped WGM resonator, with the particular aim of studying the case of pairs of modes exhibiting avoided crossings as the thickness of the disk changes. We finish with conclusions and an outlook in Sec. IV.

II. A SCALAR PRODUCT FOR THE RADIATION OF LEAKY MODES FROM 3D STRUCTURES

We start by obtaining the field radiated by a given leaky mode. The resulting polychromatic field is free of divergences.

A. Electromagnetic fields radiated by a leaky mode

Let us consider Fig. 1, where a closed surface in $\mathbb{R}^3$ delimits a volume D with a boundary ∂D that has continuous first derivatives. It is surrounded by an achiral, nonabsorbing, homogeneous, and isotropic background medium, which we assume to be vacuum for simplicity, but without loss of generality. Any other such surrounding medium can be readily accommodated in the formulas by replacing the vacuum permittivity and permeability with those of the medium. We assume the existence of time-dependent helical fields $\mathbf{F}_\lambda(\mathbf{r} \in \partial D, t)$, for helicity $\lambda = \pm 1$, on the boundary surface ∂D. We will later work with their monochromatic components $\mathbf{F}_\lambda(\mathbf{r}, |\mathbf{k}|)$. For fields that contain only positive frequencies,

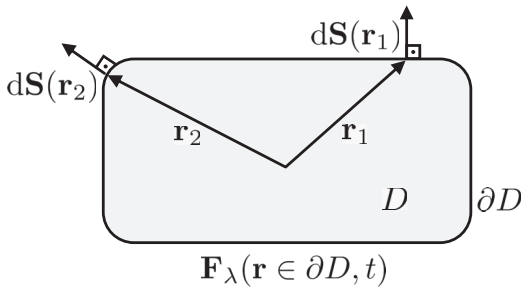

FIG. 1. A volume D in $\mathbb{R}^3$ is delimited by a closed surface ∂D with continuous first derivative. Helical fields $\mathbf{F}_{\lambda=\pm1}(\mathbf{r} \in \partial D, t)$ on the surface produce electromagnetic radiation toward the outside of D. The $\mathrm{d}\mathbf{S}(\mathbf{r})$ are outward-pointing normal vectors of the surface element at each point $\mathbf{r} \in \partial D$.

the helical fields are defined as

$$\mathbf{F}_\lambda(\mathbf{r}, t) = \sqrt{\frac{\varepsilon_0}{2}}[\mathbf{E}(\mathbf{r}, t) + \mathrm{i}\lambda Z_0 \mathbf{H}(\mathbf{r}, t)], \tag{1}$$

with vacuum permittivity ε_0, vacuum impedance Z_0, time and spatially dependent complex electric field $\mathbf{E}(\mathbf{r}, t)$, and complex magnetic field $\mathbf{H}(\mathbf{r}, t)$. Alternatively, the complex $\mathbf{B}(\mathbf{r}, t)$ field can be used instead of $\mathbf{H}(\mathbf{r}, t)$ in Eq. (1) by the substitution $Z_0\mathbf{H}(\mathbf{r}, t) \to c_0\mathbf{B}(\mathbf{r}, t)$, where c_0 is the speed of light in vacuum. The helical fields split any electromagnetic field into its left and right circular polarization handedness, with $\lambda = 1$ and $\lambda = -1$, respectively.

An expression for the scalar product between radiation fields that only involves integrals of the fields over closed spatial surfaces was recently derived [39]. In particular, the $\mathbf{F}_\lambda(\mathbf{r} \in \partial D, |\mathbf{k}|)$ appear in the expressions for the number of photons $\langle f|f\rangle$ and energy $\langle f|\mathrm{H}|f\rangle$ of a given field $|f\rangle$, which can be computed as integrals on a closed boundary [see Ref. [39], Eqs. (19) and (21)]:

$$\langle f|f\rangle = \sum_{\lambda=\pm1}(-\mathrm{i}\lambda)\int_{>0}^{\infty}\frac{\mathrm{d}|\mathbf{k}|}{\hbar c_0|\mathbf{k}|} \times \int_{\mathbf{r}\in\partial D}\mathrm{d}\mathbf{S}(\mathbf{r})\cdot[\mathbf{F}^*_\lambda(\mathbf{r}, |\mathbf{k}|)\times\mathbf{F}_\lambda(\mathbf{r}, |\mathbf{k}|)], \tag{2}$$

$$\langle f|\mathrm{H}|f\rangle = \sum_{\lambda=\pm1}(-\mathrm{i}\lambda)\int_{>0}^{\infty}\mathrm{d}|\mathbf{k}| \times \int_{\mathbf{r}\in\partial D}\mathrm{d}\mathbf{S}(\mathbf{r})\cdot[\mathbf{F}^*_\lambda(\mathbf{r}, |\mathbf{k}|)\times\mathbf{F}_\lambda(\mathbf{r}, |\mathbf{k}|)], \tag{3}$$

where $\hbar$ is Planck's constant divided by 2π, H is the energy operator, $\mathrm{d}\mathbf{S}(\mathbf{r})$ is the infinitesimal surface element at the position $\mathbf{r}$, and the integral is over any piecewise smooth surface ∂D enclosing a compact volume containing the sources of radiation.

The fact that electromagnetic fields on a boundary act as sources of radiation fields is well known in electromagnetism (see, e.g., Ref. [40] and Ref. [41], Chap. 5). The components of the electric and magnetic fields tangential to the surface uniquely determine the whole field outside the enclosed volume. This enables us to obtain the field radiated by a given leaky mode. It is important to note that the boundary ∂D does not need to be twice continuously differentiable as stated

in, e.g., Ref. [40]; rather, once continuously differentiable is enough ([41], Chap. 5), because Maxwell's equations for helical fields only contain first-order derivatives ([41], §1-2.3). This condition increases the class of surfaces to which the results apply from "continuous curvature" surfaces, such as an ellipsoid, to "continuous tangent" surfaces, such as a disk with rounded corners.

Let us now assume that the boundary ∂D in Fig. 1 is the boundary of an object, and that the electromagnetic eigenmodes of the object are available to us. Such eigenmodes will, in general, be leaky, and each of those modes with finite lifetimes can be characterized by spatial field profiles $\{\boldsymbol{\mathcal{E}}(\mathbf{r}), \boldsymbol{\mathcal{H}}(\mathbf{r})\}$ and complex frequencies $\omega = \Omega - \mathrm{i}\Gamma$, with $\{\Omega, \Gamma\} \in \mathbb{R}^+$. Eigenmodes come in conjugate pairs ([28], Sec. 2.3): If there exists a leaky mode with complex frequency $\omega = \Omega - \mathrm{i}\Gamma$ and modal fields $\boldsymbol{\mathcal{E}}(\mathbf{r})$ and $\boldsymbol{\mathcal{H}}(\mathbf{r})$, then there exists another leaky mode with complex frequency $-\omega^*$ and modal fields $\boldsymbol{\mathcal{E}}^*(\mathbf{r})$ and $\boldsymbol{\mathcal{H}}^*(\mathbf{r})$. From now on, and unless otherwise specified, we assume that $\mathbf{r}$ is a point on the surface of the object.

We want to obtain the $\mathbf{F}_\lambda(\mathbf{r}, |\mathbf{k}|)$ that specifies a physical radiation field. Importantly, the $\mathbf{F}_\lambda(\mathbf{r}, |\mathbf{k}|)$ must meet the condition

$$\mathbf{F}_\lambda(\mathbf{r}, |\mathbf{k}|) = \mathbf{F}^*_\lambda(\mathbf{r}, -|\mathbf{k}|), \tag{4}$$

because in electromagnetism the same information must be contained in the two sides of the real frequency axis ([42], §3.1) After a two-sided Fourier transform, the condition in Eq. (4) ensures $(\mathbf{r}, t)$-dependent real-valued fields.

We advance toward the specification of the $\mathbf{F}_\lambda(\mathbf{r}, |\mathbf{k}|)$ for leaky modes by considering the complex frequencies ω and $-\omega^*$ as the two poles of a complex vectorial function $\mathbf{F}_\lambda(\mathbf{r}, z \in \mathbb{C})$, whose respective residues are the helical combinations of the electric and magnetic modal fields

$$\begin{aligned} \omega = \Omega - \mathrm{i}\Gamma\,, \quad \mathbf{M}_\lambda(\mathbf{r}) &= \sqrt{\frac{\varepsilon_0}{2}}[\boldsymbol{\mathcal{E}}(\mathbf{r}) + \mathrm{i}\lambda Z_0 \boldsymbol{\mathcal{H}}(\mathbf{r})]\,, \\ -\omega^* = -\Omega - \mathrm{i}\Gamma\,, \quad \mathbf{M}^*_\lambda(\mathbf{r}) &= \sqrt{\frac{\varepsilon_0}{2}}[\boldsymbol{\mathcal{E}}(\mathbf{r}) + \mathrm{i}\lambda Z_0 \boldsymbol{\mathcal{H}}(\mathbf{r})]^*\,. \end{aligned} \tag{5}$$

At first sight, and in light of Eq. (1), $\mathbf{M}^*_\lambda(\mathbf{r}) = \sqrt{\frac{\varepsilon_0}{2}}[\boldsymbol{\mathcal{E}}^*(\mathbf{r}) - \mathrm{i}\lambda Z_0 \boldsymbol{\mathcal{H}}^*(\mathbf{r})]$ seems to be a field with helicity $-\lambda$, but this is not so: such field is also a field with helicity λ because the definition of handedness changes sign with the sign of the real part of the frequency ([43], p. 210, and [42], Sec. 3.1).

The sought-after $\mathbf{F}_\lambda(\mathbf{r}, |\mathbf{k}|)$ can be obtained using the Mittag-Leffler theorem ([38], p. 515), which allows one to expand a function $f(z)$ of a complex variable z as

$$f(z) = f(0) + \sum_{n=1}^{\infty} b_n \left(\frac{1}{z - z_n} + \frac{1}{z_n} \right). \tag{6}$$

For the expansion to hold, $f(z)$ should be analytical everywhere, excluding infinity and a set of discrete points z_n with residues b_n, and $|f(z)/z| \to 0$ as $|z| \to \infty$. We assume that each scalar component of the vectors $\mathbf{F}_\lambda(\mathbf{r}, z)$ meets such conditions. This kind of assumption underlies the common use of the Mittag-Leffler theorem in the context of resonant modes ([8], Sec. 2.3). One can then write

$$\begin{aligned} \mathbf{F}_\lambda(\mathbf{r}, k) = \mathbf{F}_\lambda(\mathbf{r}, 0) + \frac{\mathrm{i}c_0}{\sqrt{2\pi}} \\ \times \left[\frac{\mathbf{M}_\lambda(\mathbf{r})}{c_0 k - \omega} + \frac{\mathbf{M}_\lambda(\mathbf{r})}{\omega} + \frac{\mathbf{M}^*_\lambda(\mathbf{r})}{c_0 k + \omega^*} - \frac{\mathbf{M}^*_\lambda(\mathbf{r})}{\omega^*} \right], \end{aligned} \tag{7}$$

where $k \in \mathbb{R}$. The expression in Eq. (7) meets the requirement in Eq. (4).

For $\mathbf{F}_\lambda(\mathbf{r}, k)$ to be suitable for the inverse Fourier transform, it must vanish as $k \to \pm\infty$. We are hence led to set

$$\mathbf{F}_\lambda(\mathbf{r}, 0) = -\frac{\mathrm{i}c_0}{\sqrt{2\pi}} \left[\frac{\mathbf{M}_\lambda(\mathbf{r})}{\omega} - \frac{\mathbf{M}^*_\lambda(\mathbf{r})}{\omega^*} \right]. \tag{8}$$

Finally, since we are interested in $k = |\mathbf{k}| > 0$, we reach

$$\mathbf{F}_\lambda(\mathbf{r}, |\mathbf{k}|) = \frac{\mathrm{i}c_0 \mathbf{M}_\lambda(\mathbf{r})}{\sqrt{2\pi}(c_0|\mathbf{k}| - \omega)} + \frac{\mathrm{i}c_0 \mathbf{M}^*_\lambda(\mathbf{r})}{\sqrt{2\pi}(c_0|\mathbf{k}| + \omega^*)}. \tag{9}$$

Real-valued time-domain fields at each point $\mathbf{r}$ of the surface of the object can be obtained with the inverse Fourier transform,

$$\begin{aligned} \mathbf{F}_\lambda(\mathbf{r}, t) &= \int_{-\infty}^{\infty} \frac{\mathrm{d}k}{\sqrt{2\pi}} \mathbf{F}_\lambda(\mathbf{r}, k) \exp(-\mathrm{i}c_0 k t) \\ &= 2\mathrm{Re}\left\{ \int_0^{\infty} \frac{\mathrm{d}|\mathbf{k}|}{\sqrt{2\pi}} \mathbf{F}_\lambda(\mathbf{r}, |\mathbf{k}|) \exp(-\mathrm{i}c_0|\mathbf{k}|t) \right\}, \end{aligned} \tag{10}$$

which results in

$$\begin{aligned} \mathbf{F}_\lambda(\mathbf{r}, t) = [\mathbf{M}_\lambda(\mathbf{r}) \exp(-\mathrm{i}\Omega t) + \mathbf{M}^*_\lambda(\mathbf{r}) \exp(\mathrm{i}\Omega t)] \\ \times \exp(-\Gamma t) u(t), \end{aligned} \tag{11}$$

where $u(t)$ is the Heaviside step function.

The Heaviside function avoids the amplification that occurs in $\exp(-\Gamma t)$ for $t < 0$ while keeping the damping that occurs for $t > 0$. Moreover, and importantly, the fields $\mathbf{F}_\lambda(\mathbf{r}, |\mathbf{k}|) \exp(-\mathrm{i}c_0|\mathbf{k}|t)$ result in radiated fields that decay as $1/|\mathbf{r}|$ outside the resonator when $|\mathbf{r}| \to \infty$ [see Ref. [40], Eq. (35)] also avoiding the divergence of the modal fields as $|\mathbf{r}|$ grows. Hence, the presented strategy avoids the two exponential growths of the modal field outside the resonator, as $t \to -\infty$, and as $|\mathbf{r}| \to \infty$, which have been tied to each other by causality [26]. Here, the wave numbers of the radiation fields are always real. In contrast, taking the complex eigenfrequency to imply a complex wave number causes the field outside the resonator to grow exponentially as $|\mathbf{r}|$ increases. While such growing fields are being used for expanding scattered fields, typically in the monochromatic case, the exponential growth is clearly incompatible with a physical emission.

The appearance of $u(t)$ has the following physical interpretation. The surface fields specified in Eq. (9) or Eq. (11) will radiate an outgoing polychromatic pulse. Such a pulse is the radiative decay of energy stored inside the object by that given conjugate pair of leaky modes. The time $t = 0$ is the start of the emission. The procedure that leads us to Eq. (9) does not make any assumption regarding how the energy was previously acquired by the leaky modes. From now on, when we refer to a leaky mode, we mean one such conjugate pair.

We note that, even though the surface fields that act as sources must be defined on the surrounding medium, and $\{\boldsymbol{\mathcal{E}}(\mathbf{r}), \boldsymbol{\mathcal{H}}(\mathbf{r}), \boldsymbol{\mathcal{E}}^*(\mathbf{r}), \boldsymbol{\mathcal{H}}^*(\mathbf{r})\}$ are the fields inside the object, this is not a problem because the tangential components of the electric and magnetic fields are continuous at the interface between the object and the surrounding medium. The surface integrals in Eqs. (2) and (3) ensure that only the components tangential to the surface affect the result. In this way, the potentially complicated material functions characterizing the object, and their derivatives, will not appear in the expression for the scalar product that we propose in the next section, in contrast to many of the existing expressions.

There are many computational strategies for obtaining the $\{\mathbf{M}_\lambda(\mathbf{r}),\ \omega\}$ ([28], Sec. 3). For example, for sufficiently small 3D objects, the leaky modes can be obtained with software packages such as JCMSUITE [44], LUMERICAL [45], or COMSOL [46], to name just a few.

B. The cross-energy scalar product

Equation (2) can be used to compute the number of photons of a leaky mode by inserting the monochromatic components from Eq. (9). However, there are difficulties in evaluating the corresponding expression for a scalar product between two leaky modes $\langle f|g\rangle$. If we instead focus on the expression for the radiated energy, we find that the cross-energy $\langle f|\mathrm{H}|g\rangle$ between arbitrary modes f and g meets the requirements of a scalar product, which can be readily verified using the fact that the energy operator H is self-adjoint. The use of a cross-energy scalar product is reminiscent of the scalar product derived from the Poynting vector for the propagating modes of waveguides [47,48], which can be used to investigate the orthogonality between the modes [49]. This motivates us to use $\langle f|\mathrm{H}|g\rangle$ as the scalar product for leaky modes. It is obtained by inserting Eq. (9) into Eq. (3), and we call it the cross-energy scalar product:

$$
\begin{aligned}
\langle f|\mathrm{H}|g\rangle &= \sum_{\lambda=\pm1}(-\mathrm{i}\lambda)\int_{>0}^{\infty}\mathrm{d}|\mathbf{k}|\int_{\mathbf{r}\in\partial D}\mathrm{d}\mathbf{S}(\mathbf{r})\cdot[\mathbf{F}_\lambda(\mathbf{r},|\mathbf{k}|)^*\times\mathbf{G}_\lambda(\mathbf{r},|\mathbf{k}|)]\\
&= \sum_{\lambda=\pm1}(-\mathrm{i}\lambda)\frac{c_0^2}{2\pi}\left\{\int_{>0}^{\infty}\mathrm{d}|\mathbf{k}|\frac{1}{(c_0|\mathbf{k}|-\omega_f^*)}\frac{1}{(c_0|\mathbf{k}|-\omega_g)}\int_{\mathbf{r}\in\partial D}\mathrm{d}\mathbf{S}(\mathbf{r})\cdot[\mathbf{M}^*_{\lambda,f}(\mathbf{r})\times\mathbf{M}_{\lambda,g}(\mathbf{r})]\right.\\
&\quad+\int_{>0}^{\infty}\mathrm{d}|\mathbf{k}|\frac{1}{(c_0|\mathbf{k}|-\omega_f^*)}\frac{1}{(c_0|\mathbf{k}|+\omega_g^*)}\int_{\mathbf{r}\in\partial D}\mathrm{d}\mathbf{S}(\mathbf{r})\cdot[\mathbf{M}^*_{\lambda,f}(\mathbf{r})\times\mathbf{M}^*_{\lambda,g}(\mathbf{r})]\\
&\quad+\int_{>0}^{\infty}\mathrm{d}|\mathbf{k}|\frac{1}{(c_0|\mathbf{k}|+\omega_f)}\frac{1}{(c_0|\mathbf{k}|-\omega_g)}\int_{\mathbf{r}\in\partial D}\mathrm{d}\mathbf{S}(\mathbf{r})\cdot[\mathbf{M}_{\lambda,f}(\mathbf{r})\times\mathbf{M}_{\lambda,g}(\mathbf{r})]\\
&\quad\left.+\int_{>0}^{\infty}\mathrm{d}|\mathbf{k}|\frac{1}{(c_0|\mathbf{k}|+\omega_f)}\frac{1}{(c_0|\mathbf{k}|+\omega_g^*)}\int_{\mathbf{r}\in\partial D}\mathrm{d}\mathbf{S}(\mathbf{r})\cdot[\mathbf{M}_{\lambda,f}(\mathbf{r})\times\mathbf{M}^*_{\lambda,g}(\mathbf{r})]\right\},
\end{aligned}
\tag{12}
$$

where the subscripts f and g denote the two considered modes. Appendix A shows that the result of the $\mathrm{d}|\mathbf{k}|$ integral can be obtained in closed form, with which one obtains

$$
\begin{aligned}
\langle f|\mathrm{H}|g\rangle &= \frac{c_0}{2\pi}\sum_{\lambda=\pm1}(-\mathrm{i}\lambda)\frac{\mathrm{Log}(-\omega_f^*)-\mathrm{Log}(-\omega_g)}{-\omega_f^*+\omega_g}\int_{\mathbf{r}\in\partial D}\mathrm{d}\mathbf{S}(\mathbf{r})\cdot[\mathbf{M}^*_{\lambda,f}(\mathbf{r})\times\mathbf{M}_{\lambda,g}(\mathbf{r})]\\
&\quad+\frac{c_0}{2\pi}\sum_{\lambda=\pm1}(-\mathrm{i}\lambda)\frac{\mathrm{Log}(-\omega_f^*)-\mathrm{Log}(\omega_g^*)}{-\omega_f^*-\omega_g^*}\int_{\mathbf{r}\in\partial D}\mathrm{d}\mathbf{S}(\mathbf{r})\cdot[\mathbf{M}^*_{\lambda,f}(\mathbf{r})\times\mathbf{M}^*_{\lambda,g}(\mathbf{r})]\\
&\quad+\frac{c_0}{2\pi}\sum_{\lambda=\pm1}(-\mathrm{i}\lambda)\frac{\mathrm{Log}(\omega_f)-\mathrm{Log}(-\omega_g)}{\omega_f+\omega_g}\int_{\mathbf{r}\in\partial D}\mathrm{d}\mathbf{S}(\mathbf{r})\cdot[\mathbf{M}_{\lambda,f}(\mathbf{r})\times\mathbf{M}_{\lambda,g}(\mathbf{r})]\\
&\quad+\frac{c_0}{2\pi}\sum_{\lambda=\pm1}(-\mathrm{i}\lambda)\frac{\mathrm{Log}(\omega_f)-\mathrm{Log}(\omega_g^*)}{\omega_f-\omega_g^*}\int_{\mathbf{r}\in\partial D}\mathrm{d}\mathbf{S}(\mathbf{r})\cdot[\mathbf{M}_{\lambda,f}(\mathbf{r})\times\mathbf{M}^*_{\lambda,g}(\mathbf{r})],
\end{aligned}
\tag{13}
$$

where Log denotes the principal value of the complex logarithm. In the following section, we use the cross-energy scalar product to study the modes of a disk resonator as the thickness of the disk changes. A disk is a rather symmetric object. However, the scalar product applies very generally. In this respect, and besides the standard conditions on the embedding medium specified at the beginning of Sec. II A, the conditions for applicability are that the surface of the object must be continuously differentiable once, and enclose a compact volume. Any finite object without sharp edges meets these conditions. Compositions of finite objects are also covered. For example, let us consider a plasmonic gap mode between two spheres. Taking the two spheres as a composite object, the enclosing surface can be chosen to be the surfaces of the spheres except for a connection between the two, for example, by a tube, whose cross section can

be made arbitrarily small. It is easy to see that the absence of field sources inside the tube would make the surface integrals in Eq. (13) vanish over the tube, so only the integrals over the spheres would contribute. The plasmonic gap mode would then be treated as any other mode of the composite system.

One of the uses of Eq. (13) is to normalize the modes dividing them by $\sqrt{\langle f|\mathrm{H}|f\rangle}$. There exist several different expressions for normalizing quasi-normal modes, such as, for example, Ref [16], Eq. (4); Ref. [27], Eq. (22); or Ref. [8], Eq. (20). Detailed comparisons of these and other alternatives can be found in Ref. [28], Sec. 4, and Ref. [8], Sec. 4. Typically, the expressions contain volume and surface integrals in a computational domain containing the resonator. The divergent behavior of the modal fields is the main complication, and in some approaches, compromises the convergence of the results. In some cases, such divergence is handled by including perfectly matched layers at the edges of the domain, and then also integrating over them. Many of the expressions contain the material parameters of the resonator and their derivatives with respect to frequency. In contrast, our approach results in a single integral across the surface of the object, avoiding the divergent behavior of the modal fields outside the object. Moreover, the integral does not depend on the material parameters of the resonator. We think that these features are advantageous.

III. APPLICATION TO WHISPERING GALLERY RESONATORS

A. The modes of a disk

Here, we consider a WGM resonator, modeled as a disk of radius 25 µm and thickness changing from 1.8 µm to 3.1 µm. The material of the disk resonator is assumed to have real permittivity $\varepsilon^{\mathrm{r}}_{\mathrm{res}} = (1.481)^2$ and imaginary permittivity $\varepsilon^{\mathrm{i}}_{\mathrm{res}} = 10^{-4}$, and the surrounding permittivity of air $\varepsilon_{\mathrm{sur}} = (1.000\,275)^2$, following Ref. [37]. Note that the surrounding medium here is not vacuum as assumed in the construction of the fields before. However, $\varepsilon_{\mathrm{sur}}$ differs only marginally from unity, and we can neglect its influence, since the results are virtually identical to the vacuum case. The electric and magnetic fields and the resonance frequencies are computed with the finite element method (FEM) simulation software JCMSUITE. It solves the resonant mode problem by finding electric and magnetic fields $[\boldsymbol{\mathcal{E}}_f(\mathbf{r}), \boldsymbol{\mathcal{H}}_f(\mathbf{r})]$ of the modes f and corresponding eigenvalues $\omega_f = \Omega_f - \mathrm{i}\Gamma_f$, satisfying the time-harmonic Maxwell equations with outgoing boundary conditions in a source-free medium. In our case, the numerical implementation exploits the rotational symmetry of the disk with respect to the z axis, and the eigenmode computation is reduced to a two-dimensional problem, expressed in cylindrical coordinates in the plane $[\rho = \sqrt{x^2+y^2}, \varphi = \mathrm{arctan2}(y,x) = 0, z]$, as visualized in Fig. 2. At any point on the disk, the fields of a given solution (in Cartesian coordinates) obey

$$\boldsymbol{\mathcal{E}}_f^{(m^f)}(\rho\cos\varphi, \rho\sin\varphi, z) = \mathrm{R}\cdot\boldsymbol{\mathcal{E}}_f^{(m^f)}(\rho, 0, z)\mathrm{e}^{\mathrm{i}m^f\varphi}, \quad (14)$$

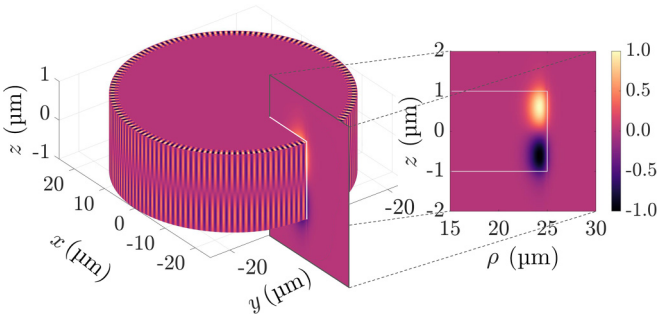

FIG. 2. The radial component of the real part of the electric field of the fundamental mode on the disk surface (left). Because of the azimuthal symmetry, we consider resonant modes computed in a slice of the disk in the xz plane [projected on the right, in cylindrical coordinates $(\rho, \varphi = 0, z)$]. The discretization in the radial direction is nonuniform, and finer close to the rim. The field decreases by several orders of magnitude at the borders of the chosen computational domain. For the sake of visibility, the domain in the figure differs from the size of the actual computational domain, and the scale of the z axis is different from that of the other two axes.

and similarly for $\boldsymbol{\mathcal{H}}_f^{(m^f)}$, with azimuth φ, integer azimuthal mode number m^f, and the rotation matrix[1] [44]

$$\mathrm{R} = \begin{bmatrix} \cos\varphi & -\sin\varphi & 0 \\ \sin\varphi & \cos\varphi & 0 \\ 0 & 0 & 1 \end{bmatrix}. \quad (15)$$

The fields $(\boldsymbol{\mathcal{E}}_f^{(m^f)}, \boldsymbol{\mathcal{H}}_f^{(m^f)})$ can be used to construct (helical) modal fields $\mathbf{M}_{\lambda,f}^{(m^f)}(\mathbf{r})$ following the definition in Eq. (5), and then the corresponding $\mathbf{F}_{\lambda}^{(m^f)}(\mathbf{r}, |\mathbf{k}|)$ in Eq. (9). It is straightforward to show that under the cross-energy scalar product two modes are orthogonal unless $|m^f| = |m^g|$: For instance, the surface integral in the first line of Eq. (13) contains a term $\mathrm{e}^{\mathrm{i}(m^g - m^f)\varphi}$, which makes the integral vanish identically if $m^g \neq m^f$. Importantly, modes of opposite azimuthal mode number, that is, for $m^f = -m^g$, can be nonorthogonal. This is because the monochromatic components in Eq. (9) contain the modal fields and their complex conjugate and, therefore, combine terms of azimuthal dependence $\mathrm{e}^{\pm\mathrm{i}m\varphi}$. This can be understood as a direct consequence of Eq. (4), which is a necessary condition for real-valued fields in $(\mathbf{r}, t)$.

This nonorthogonality motivates one to find a different way to build modes for the analysis of the resonator. To such end, we consider a mirror reflection across a plane that contains the symmetry axis of the disk, for example, M_y, which acts by changing the sign of the y coordinate. Since the material of the disk is achiral, such operation is a symmetry of the disk, which means that applying it to a given leaky mode produces a potentially different mode, but with the same modal frequency. For cylindrically symmetric systems that are mirror symmetric with respect to a plane that includes the axis of rotation, such as the disk, the corresponding modal field $\mathbf{M}_{\lambda,f}^{(-m^f)}(\mathbf{r})$ is readily

[1]Note that JCMSUITE uses a different convention where the y axis is the axis of rotational symmetry.

found by the mirror reflection, which transforms the fields in Eq. (14) into those that exhibit an azimuthal dependence of $e^{i(-m^f)\varphi}$. See Appendix B for details. The fields obtained in this way for the disk resonator match the ones numerically computed for $-m^f$ precisely, up to phase factors, which are explained by the rotational degree of freedom in choosing a mirror plane that contains the symmetry axis. It therefore suffices to compute the fields only for one sign of m.

We show in Appendix B that the leaky modes constructed with Eq. (9), using the even and odd ($\tau_y = \pm 1$) combinations

$$\mathbf{M}^{(\tau_y)}_{\lambda,f}(\mathbf{r}) = \frac{1}{\sqrt{2}}\left(\mathbf{M}^{(m^f)}_{\lambda,f}(\mathbf{r}) + \tau_y \mathbf{M}^{(-m^f)}_{\lambda,f}(\mathbf{r})\right), \tag{16}$$

are orthogonal when their τ_y values are not the same, independently of the values of their azimuthal numbers. Note that the mirror transformation relates the fields with opposite signs of λ, since it changes the handedness of the fields. The combinations in Eq. (16) result in leaky modes that are eigenstates of M_y with eigenvalue τ_y. They are also eigenstates of rotations along the z axis by discrete angles $\pi/|m^f|$. We will work with the M_y-symmetric modes constructed with Eq. (16), defined for $\tau_y = \pm 1$ and, without loss of generality, with $m^f \geqslant 0$.

Let us now advance to the study of the modes of the disk resonator, selecting $|m| = 139$ to match Ref. [37]. Due to the field localization near the resonator rim, the region from which the fields are extracted can be limited to $[19.5, 27.0]$ μm along ρ and $[-3, 3]$ μm in the z direction. The target relative precision of resonance frequencies is set to 10^{-6}, and an adaptive mesh refinement scheme with two maximum refinement steps is used. The computational domain is surrounded by perfectly matched layers (PMLs) [44].

The resonance frequencies of the modes change with varying thickness of the disk. The real parts of the frequencies of the first ten modes emerging from the FEM computation are plotted in Fig. 3 for disk thicknesses ranging from 1.8 to 3.1 μm. The corresponding imaginary parts can be found in Appendix C. It is known from symmetry analysis in Ref. [37] that some modes exhibit crossings over the course of the varying disk thickness, and some exhibit avoided crossings, also called anticrossings. In particular, the disk is invariant under the mirror reflection M_z: $z \mapsto -z$. Then, the electric field distribution $\boldsymbol{\mathcal{E}}_f(\mathbf{r})$ of each mode is an eigenstate of such reflection with eigenvalue $\tau_z = 1$ or $\tau_z = -1$, and the magnetic field distribution $\boldsymbol{\mathcal{H}}_f(\mathbf{r})$ is also an eigenstate of the reflection $z \mapsto -z$ with the opposite eigenvalue $-\tau_z$. The sign difference is due to the polar and axial character of electric and magnetic fields, respectively. For example, the field in Fig. 2 transforms with an eigenvalue $\tau_z = -1$. Modes of opposite τ_z cross and modes with the same τ_z anticross, as seen in Ref. [37]. The anticrossings are marked with gray circles in Fig. 3.

It is important to highlight that crossings affect the ordering of the modes. As a result of the FEM computation, the modes are sorted independently for every disk thickness and assigned a spectral order number according to their increasing real part of the resonance. Such spectral order naturally swaps the labels for modes that cross as the thickness of the disk increases, and, therefore, does not reflect their true order. In our case, however, this can be circumvented by considering

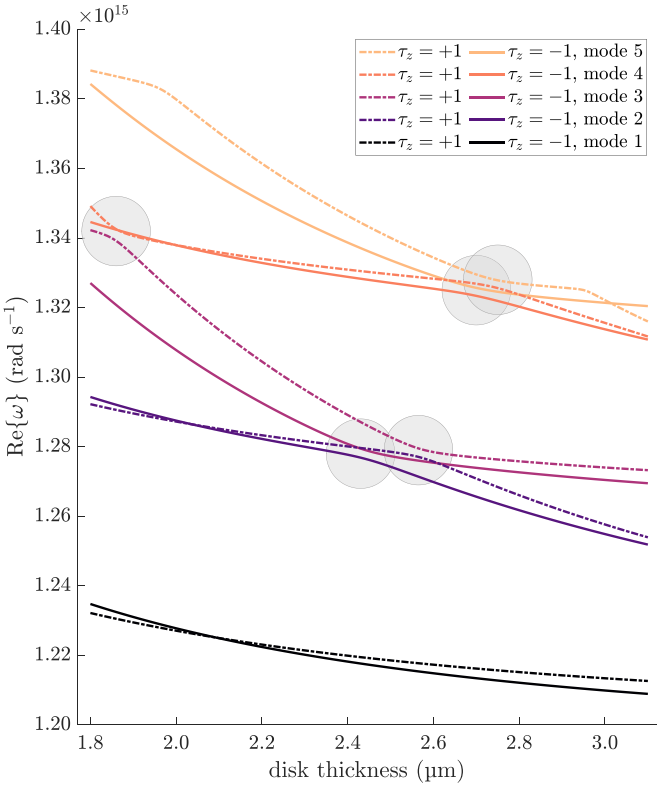

FIG. 3. Real part of the angular resonance frequency of the five pairs of lowest-order modes as a function of disk thickness. Solid lines follow modes with negative τ_z, and dashed lines mark the resonance frequencies of modes with positive τ_z, where τ_z is the eigenvalue of the mode upon a $z \mapsto -z$ mirror transformation. Modes of equal τ_z undergo avoided crossings at the spots marked with gray circles.

the spectral order of modes separately for different τ_z, since crossings only occur between modes of opposite τ_z. More complex resonators may not allow such "manual" tracking. Then, the cross-energy scalar product between eigenmodes can be used as a general way to track the modes as some resonator parameters change smoothly. This can be done by projecting the radiation field of each mode for a given set of parameters onto the radiation field of each mode in the next set and connecting a given mode of the first set to the mode of the second set, which results in the maximum value of their mutual projection.

B. The cross-energy scalar product: Similarity between modes

We analyze the orthogonality properties of the modes as a function of the disk thickness using the following quantity:

$$|\langle \hat{f}|\mathrm{H}|\hat{g}\rangle|^2 = \frac{|\langle f|\mathrm{H}|g\rangle|^2}{\langle f|\mathrm{H}|f\rangle \langle g|\mathrm{H}|g\rangle}, \tag{17}$$

where the normalization of each mode is considered so that each normalized mode radiates the same amount of energy: $|\hat{f}\rangle = |f\rangle / \sqrt{\langle f|\mathrm{H}|f\rangle}$ and $|\hat{g}\rangle = |g\rangle / \sqrt{\langle g|\mathrm{H}|g\rangle}$.

For the case of a cylindrically symmetric system such as the disk, the expression in Eq. (13) is further simplified by reducing the two-dimensional surface integrals to

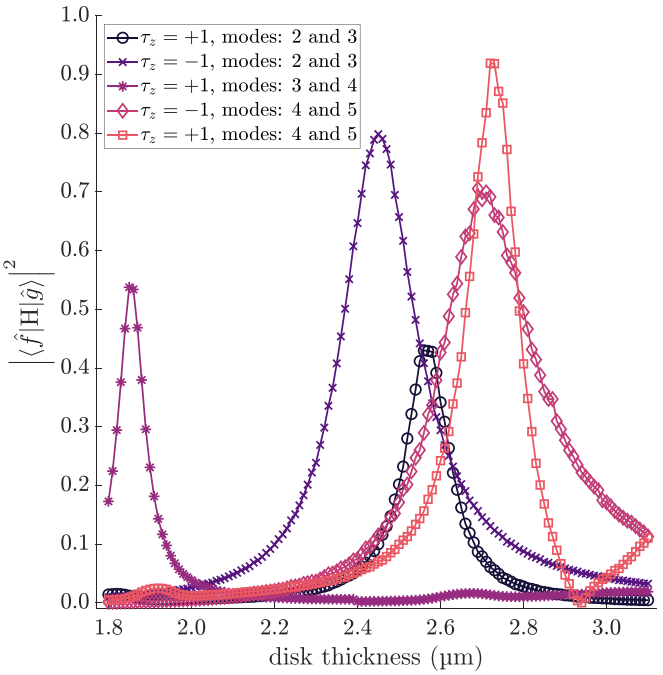

FIG. 4. Result of Eq. (17) for chosen pairs of modes as a function of disk thickness. The peaks coincide with the thickness for which the anticrossing occurs between the particular modes, as marked in Fig. 3.

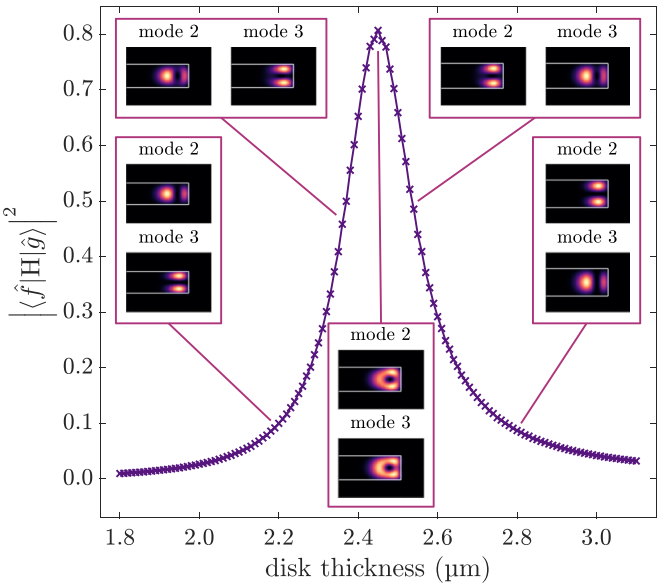

FIG. 5. Result of Eq. (17) for the modes of spectral order 2 and 3 and $\tau_z = -1$ as a function of the disk thickness. The inset figures show the normalized energy density distribution of the modal fields at particular values of the thickness. The field distributions plotted here are closely related to the ones in Fig. 3 of Ref. [37].

one-dimensional (1D) contour integrals. See Appendix B for details. The integral is then computed using the trapezoidal rule over the contour $\mathcal{C}$ drawn with a white line in the projection in Fig. 2. The discretization of the contour has been chosen with enough resolution so that the simple trapezoidal rule produces satisfactory results, as shown by a convergence analysis. Higher-order quadrature rules can be beneficial for reducing the number of sampling points for a given desired accuracy, in particular for asymmetric resonators where the integrals must be carried out over the whole surface of the resonator [35,36]. We choose the dimensions of the contour (the height and width) to be 2% larger than the actual contour of the $\varphi = 0$ slice of the disk to avoid regions of numerical artifacts in the simulated fields, which are found near the edges of the disk resonator. Sampling the fields slightly outside the resonator technically means sampling fields that feature an exponentially divergent behavior toward spatial infinity due to being associated with a complex wave number. However, the rate of divergence is related to the radiative damping of the resonant modes. For fairly high-quality resonances, indicated by the ratio Ω/Γ, in the order of 10^5 for the modes discussed here, the exponential divergence is slow enough to be negligible this close to the resonator surface. Correspondingly, this is a good approximation to the desired fields at the surface of the disk. The contour is discretized finer close to the rim of the disk, where the fields are localized.

The modes that cross, having opposite τ_z, are orthogonal under the cross-energy scalar product. This is readily seen by splitting the surface integrals in Eq. (13) into their $z > 0$ and $z < 0$ pieces, whose sum (including the sum over λ) cancels out if the modes have opposite τ_z. Figure 4 shows the result of Eq. (17) for selected pairs of modes of the same τ_z and same parameter $\tau_y = 1$ as introduced in Eq. (16). As explained in Appendix B, the values of the scalar products for this example are virtually the same for both signs of τ_y, because the differences are of the order of the inverse of the Q factors of the modes. In the general case, the results for both values of $\tau_y = \pm 1$ should be considered. Each line of Fig. 4 shows how a prominent peak grows as the real frequencies of that particular pair of modes get close to each other in Fig. 3. The position of the peak neatly aligns with the thicknesses at which the two modes anticross, which here translates into enlarged nonorthogonality of the respective modal radiations. The origin of this nonorthogonality is further elucidated by the example singled out in Fig. 5, which shows the value of Eq. (17) for a pair of modes of $\tau_z = -1$. The inset figures present the electric field density profiles of the investigated modes for chosen values of disk thickness. As the disk thickness increases, the profiles deform, reach approximately the same shape, and then separate but with interchanged field profiles and modal numbers $(2, 3) \leftrightarrow (3, 2)$. The cross-energy scalar product peaks exactly when the two mode profiles have maximum overlap. The cross-energy scalar product can be seen as a measure of the similarity between the radiation fields of two modes, in particular in the far field. Under such interpretation, Fig. 4 shows that, at the anticrossing points, the similarity between the radiation fields depends on which pair of modes is considered. It is reassuring that the radiations are most similar exactly when the modal eigenfields inside the resonator are most similar.

IV. CONCLUSION AND OUTLOOK

We have put forward a scalar product for the study of optical resonators using the conformally invariant scalar product

for radiation fields. We showed how any given resonant mode, obtained, for example, from a Maxwell solver, can be used to determine fields on the surface of the resonator that produce a finite-energy polychromatic emission free of divergences. Then, we identified a cross-energy expression between the radiations of any two given modes as a suitable scalar product. The application to the modes of a disk-shaped WGM resonator showed that the cross-energy scalar product produces physically relevant information, as it predicts the anticrossing between modes upon smooth changes of the geometrical parameters of the disk and provides information regarding the ability to distinguish between the radiation patterns of different leaky modes.

The cross-energy scalar product introduced between radiation fields offers a robust and generalizable method for tracking resonant modes as the parameters of a resonator vary continuously. This is accomplished by projecting the radiation field of each mode at a given parameter set onto the radiation fields of modes in the subsequent set. A correspondence between modes is then established by identifying the projection that yields the highest overlap. While in the case of a disk resonator, mode tracking can often be performed using symmetry considerations, such symmetry-based approaches may not be applicable for more complex resonator geometries. In these cases, the scalar product method provides a valuable alternative. This may serve as a tool to optimize the dimensions of the resonators to obtain a desired behavior at specific frequencies. Moreover, considering the mode profiles on the surface offers a computational advantage as it is not necessary to consider the entire volume of the resonating structure.

This work also opens a path for a different elucidation of the orthogonality and degree of asymptotic completeness of a given series of resonant modes. The same cross-energy scalar product can be used between the radiation of a given mode and any general radiation field, thereby allowing the decomposition of the latter into normalized modes.

ACKNOWLEDGMENTS

M.P.-I. acknowledges support by the NHR@KIT program. L.R. acknowledges support by the Karlsruhe School of Optics & Photonics (KSOP). This work was partially funded by the Deutsche Forschungsgemeinschaft (DFG, German Research Foundation) – Project-ID 258734477 – SFB 1173. I.F.-C. warmly thanks Philippe Lalanne and the members of his group, particularly Tong Wu, for the hospitality and illuminating discussions regarding electromagnetic eigenmodes during an academic visit in the spring of 2024. I.F.-C. and C.R. acknowledge funding by the Helmholtz Association via the Helmholtz program "Materials Systems Engineering" (MSE). We are grateful to the company JCMwave for their free provision of the FEM Maxwell solver JCMSUITE.

DATA AVAILABILITY

The data that support the findings of this article are not publicly available. The data are available from the authors upon reasonable request.

APPENDIX A: A GENERAL SIMPLIFICATION

The integrals over $|\mathbf{k}|$ in Eq. (12) can be solved analytically, using

$$\int_0^\infty \mathrm{d}x \frac{1}{x-z_1^*}\frac{1}{x-z_2} = \frac{\mathrm{Log}(-z_1^*)-\mathrm{Log}(-z_2)}{-z_1^*+z_2} \tag{A1}$$

for $z_{1,2} \notin \mathbb{R}$. Identifying x with $c_0|\mathbf{k}|$ and (z_1, z_2) with one of the combinations (ω_f, ω_g), $(\omega_f, -\omega_g^*)$, $(-\omega_f^*, \omega_g)$, and $(-\omega_f^*, -\omega_g^*)$ and using Eq. (A1) four times yields Eq. (13).

APPENDIX B: APPLICATION TO AN ACHIRAL DISK

In the case of cylindrical symmetry, the surface integrals in Eq. (13) can be rewritten using the azimuthal dependence of the modes described in Eq. (14), for example, from the first line of Eq. (13):

$$\begin{aligned}\int_{\mathbf{r}\in\partial D} \mathrm{d}\mathbf{S}(\mathbf{r}) \cdot \left[\left(\mathbf{M}_{\lambda,f}^{(m^f)}(\mathbf{r})\right)^* \times \mathbf{M}_{\lambda,g}^{(m^g)}(\mathbf{r})\right] \\ = \int_{\mathcal{C}} \mathrm{d}s\rho\hat{\mathbf{v}}(\mathbf{r}) \cdot \left[\left(\mathbf{M}_{\lambda,f}^{(m^f)}(\mathbf{r})\right)^* \times \mathbf{M}_{\lambda,g}^{(m^g)}(\mathbf{r})\right] \\ \times \int_0^{2\pi} \mathrm{d}\varphi \mathrm{e}^{\mathrm{i}(-m^f+m^g)\varphi}\,.\end{aligned} \tag{B1}$$

Here, we have written $\mathrm{d}\mathbf{S}(\mathbf{r}) = \mathrm{d}s \cdot \rho \mathrm{d}\varphi \hat{\mathbf{v}}(\mathbf{r})$ in cylindrical coordinates (ρ, φ, z), with the surface normal vector $\hat{\mathbf{v}}$. The contour $\mathcal{C}$ refers to the 1D curve defined as the $\varphi = 0$ slice of ∂D, and $\mathrm{d}s$ denotes a differential line element of $\mathcal{C}$. The integral over φ in Eq. (B1) evaluates to 2π only in the case where $m^f = m^g$, making the entire surface integral vanish otherwise.

Analogously, we can simplify the surface integral in the second line of Eq. (13), which vanishes unless $m^f = -m^g$. Note that the surface integrals in lines three and four of Eq. (13) are simply the complex conjugates of the integrals in lines two and one, respectively.

In summary, only pairs of modes satisfying $|m^f| = |m^g|$ can have a nonzero scalar product. In either case (excluding $m = 0$), the four terms in Eq. (13) are reduced to only two, with the two-dimensional surface integrals

$$\int_{\mathbf{r}\in\partial D} \mathrm{d}\mathbf{S}(\mathbf{r}) \cdot [\ldots]$$

replaced by one-dimensional line integrals

$$2\pi \int_{\mathcal{C}} \mathrm{d}s\rho\hat{\mathbf{v}}(\mathbf{r}) \cdot [\ldots]\,.$$

As explained in the main text, we can build mirror symmetric modes [Eq. (16)] by combining $\mathbf{M}_{\lambda,f}^{(m^f)}(\mathbf{r})$ fields with their mirror reflections $\mathbf{M}_{\lambda,f}^{(-m^f)}(\mathbf{r})$. In a cylindrically symmetric system that also features a plane of mirror symmetry containing the axis of rotation, $\mathbf{M}_{\lambda,f}^{(-m^f)}(\mathbf{r})$ can be obtained from $\mathbf{M}_{\lambda,f}^{(m^f)}(\mathbf{r})$ using one of the mirror symmetries of the system where the axis of rotational symmetry is contained in the mirror plane. For example, using $\mathrm{M}_y = \begin{bmatrix}1 & 0 & 0\\ 0 & -1 & 0\\ 0 & 0 & 1\end{bmatrix}$ in Cartesian

coordinates, which maps $y \mapsto -y$, we can write

$$\mathbf{M}^{(-m^f)}_{\lambda,f}(\mathbf{r}) = \mathrm{M}_y \mathbf{M}^{(m^f)}_{-\lambda,f}(\mathrm{M}_y \mathbf{r}). \tag{B2}$$

Note that Eq. (B2) relates fields of opposite helicity, in line with the fact that any mirror transformation changes an eigenstate of helicity into one of opposite helicity, or, colloquially, flips its handedness. This change of handedness can also be deduced from the transformations of the modal fields under a mirror transformation, $\boldsymbol{\mathcal{E}}_f(\mathbf{r}) \mapsto \mathrm{M}_y \boldsymbol{\mathcal{E}}_f(\mathrm{M}_y \mathbf{r})$ and $\boldsymbol{\mathcal{H}}_f(\mathbf{r}) \mapsto -\mathrm{M}_y \boldsymbol{\mathcal{H}}_f(\mathrm{M}_y \mathbf{r})$, whose difference in sign is due to the polar and axial character of electric and magnetic fields, respectively.

The above arguments can be used to show the mutual orthogonality of the even and odd modal fields introduced in Eq. (16). For the purpose of brevity, we introduce the notation

$$|f, \pm m^f\rangle \equiv \left\{\mathbf{M}^{(\pm m^f)}_{\lambda,f}(\mathbf{r}), \omega_f\right\} \tag{B3}$$

$$\left|f, \tau_y^f\right\rangle \equiv \left\{\mathbf{M}^{(\tau_y)}_{\lambda,f}(\mathbf{r}), \omega_f\right\}, \tag{B4}$$

where the fields on the right-hand side correspond to the ones in Eq. (16), and the meaning of the equivalence sign is the radiation field from the leaky modes as built with Eq. (9).

Considering the mirror transformation used to obtain the $\mathbf{M}^{(-m^f)}_{\lambda,f}(\mathbf{r})$ from $\mathbf{M}^{(m^f)}_{\lambda,f}(\mathbf{r})$, one can show that

$$\begin{aligned}\langle f, m^f|\mathrm{H}|g, -m^g\rangle &= \langle f, -m^f|\mathrm{H}|g, m^g\rangle, \text{ and}\\ \langle f, m^f|\mathrm{H}|g, m^g\rangle &= \langle f, -m^f|\mathrm{H}|g, -m^g\rangle,\end{aligned} \tag{B5}$$

and with that

$$\begin{aligned}\left\langle f, \tau_y^f\middle|\mathrm{H}\middle|g, \tau_y^g\right\rangle &= \frac{1+\tau_y^f\tau_y^g}{2}\langle f, m^f|\mathrm{H}|g, m^g\rangle\\ &\quad + \frac{\tau_y^f+\tau_y^g}{2}\langle f, -m^f|\mathrm{H}|g, m^g\rangle\\ &= \big(\langle f, m^f|\mathrm{H}|g, m^g\rangle\\ &\quad + \tau_y^f\langle f, -m^f|\mathrm{H}|g, m^g\rangle\big)\delta_{\tau_y^f,\tau_y^g},\end{aligned} \tag{B6}$$

where the Kronecker delta in the last line formalizes the orthogonality of modes with nonmatching τ_y.

The remaining τ_y^f in the last line of Eq. (B6) shows that $\langle f, \tau_y^f = 1|\mathrm{H}|g, \tau_y^g = 1\rangle$ and $\langle f, \tau_y^f = -1|\mathrm{H}|g, \tau_y^g = -1\rangle$ are, in general, different. Such difference is on the order of the inverse Q-factor of the modes. This can be seen from the prefactors involving the modal frequencies in Eq. (13).

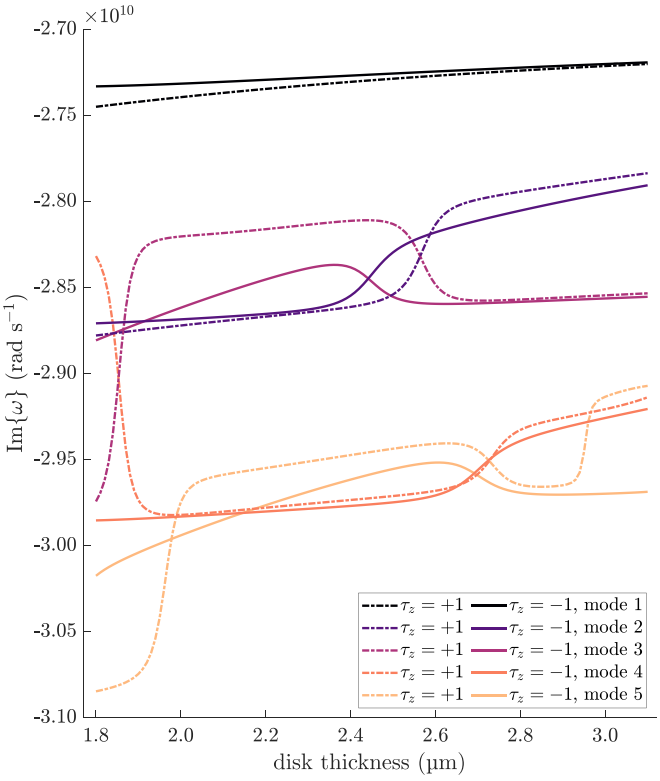

FIG. 6. Imaginary part of the angular resonance frequency of the five pairs of lowest-order modes as a function of disk thickness, corresponding to the real parts shown in Fig. 3.

For $m^f = m^g$, the term $\langle f, m^f|\mathrm{H}|g, m^g\rangle$ involves evaluating the first and fourth lines in Eq. (13), and the term $\langle f, -m^f|\mathrm{H}|g, m^g\rangle$ involves lines two and three in Eq. (13). For degenerate modes, but also for spectrally close modes, the absolute value of the ratio between the prefactors of such lines is roughly the Q factor of the modes. The relative difference between $\langle f, \tau_y|\mathrm{H}|g, \tau_y\rangle$ for different τ_y is correspondingly small for the modes of the disk that we study.

APPENDIX C: IMAGINARY PARTS OF THE MODAL RESONANCE FREQUENCIES

Complementary to the real parts shown in Fig. 3, the imaginary parts of the angular frequencies of the modes are plotted in Fig. 6. The avoided crossings marked in Fig. 3 become noticeable in this data as an exchange between the damping factors, $\Gamma = -\mathrm{Im}\{\omega\}$, of a pair of modes.

[1] K. J. Vahala, Optical microcavities, Nature (London) **424**, 839 (2003).

[2] Z. Yuan, P. C. Wu, and Y.-C. Chen, Optical resonator enhanced photovoltaics and photocatalysis: Fundamental and recent progress, Laser Photon. Rev. **16**, 2100202 (2022).

[3] Y. Zhang, Z. Yuan, Z. Qiao, D. Barshilia, W. Wang, G.-E. Chang, and Y.-C. Chen, Tunable microlasers modulated by intracavity spherical confinement with chiral liquid crystal, Adv. Opt. Mater. **8**, 1902184 (2020).

[4] V. S. Ilchenko and A. B. Matsko, Optical resonators with whispering-gallery modes—Part II: Applications, IEEE J. Sel. Top. Quantum Electron. **12**, 15 (2006).

[5] M. Loyez, M. Adolphson, J. Liao, and L. Yang, From whispering gallery mode resonators to biochemical sensors, ACS Sens. **8**, 2440 (2023).

[6] P. T. Kristensen, K. Herrmann, F. Intravaia, and K. Busch, Modeling electromagnetic resonators using quasinormal modes, Adv. Opt. Photon. **12**, 612 (2020).

[7] P. Lalanne, W. Yan, A. Gras, C. Sauvan, J.-P. Hugonin, M. Besbes, G. Demésy, M. D. Truong, B. Gralak, F. Zolla, A. Nicolet, F. Binkowski, L. Zschiedrich, S. Burger, J. Zimmerling, R. Remis, P. Urbach, H. T. Liu, and T. Weiss, Quasinormal mode solvers for resonators with dispersive materials, J. Opt. Soc. Am. A **36**, 686 (2019).

[8] C. Sauvan, T. Wu, R. Zarouf, E. A. Muljarov, and P. Lalanne, Normalization, orthogonality, and completeness of quasinormal modes of open systems: The case of electromagnetism, Opt. Express **30**, 6846 (2022).

[9] R.-C. Ge and S. Hughes, Quantum dynamics of two quantum dots coupled through localized plasmons: An intuitive and accurate quantum optics approach using quasinormal modes, Phys. Rev. B **92**, 205420 (2015).

[10] M. Kamandar Dezfouli and S. Hughes, Regularized quasinormal modes for plasmonic resonators and open cavities, Phys. Rev. B **97**, 115302 (2018).

[11] F. Binkowski, F. Betz, R. Colom, M. Hammerschmidt, L. Zschiedrich, and S. Burger, Quasinormal mode expansion of optical far-field quantities, Phys. Rev. B **102**, 035432 (2020).

[12] R. Colom, R. McPhedran, B. Stout, and N. Bonod, Modal expansion of the scattered field: Causality, nondivergence, and nonresonant contribution, Phys. Rev. B **98**, 085418 (2018).

[13] T. Wu, M. Gurioli, and P. Lalanne, Nanoscale light confinement: The Q's and V's, ACS Photonics **8**, 1522 (2021).

[14] R.-C. Ge, P. T. Kristensen, J. F. Young, and S. Hughes, Quasinormal mode approach to modelling light-emission and propagation in nanoplasmonics, New J. Phys. **16**, 113048 (2014).

[15] M. V. Gorkunov, A. A. Antonov, A. V. Mamonova, E. A. Muljarov, and Y. Kivshar, Substrate-induced maximum optical chirality of planar dielectric structures, Adv. Opt. Mater. **13**, 2402133 (2024).

[16] P. T. Kristensen, C. Van Vlack, and S. Hughes, Generalized effective mode volume for leaky optical cavities, Opt. Lett. **37**, 1649 (2012).

[17] S. Franke, S. Hughes, M. K. Dezfouli, P. T. Kristensen, K. Busch, A. Knorr, and M. Richter, Quantization of quasinormal modes for open cavities and plasmonic cavity quantum electrodynamics, Phys. Rev. Lett. **122**, 213901 (2019).

[18] N. A. Gippius, T. Weiss, S. G. Tikhodeev, and H. Giessen, Resonant mode coupling of optical resonances in stacked nanostructures, Opt. Express **18**, 7569 (2010).

[19] T. Coenen, J. Van De Groep, and A. Polman, Resonant modes of single silicon nanocavities excited by electron irradiation, ACS Nano **7**, 1689 (2013).

[20] D. Martin-Cano, H. R. Haakh, and N. Rotenberg, Chiral emission into nanophotonic resonators, ACS Photonics **6**, 961 (2019).

[21] T. Wu and P. Lalanne, Exact Maxwell evolution equation of resonator dynamics: Temporal coupled-mode theory revisited, Opt. Express **32**, 20904 (2024).

[22] F. Betz, M. Hammerschmidt, L. Zschiedrich, S. Burger, and F. Binkowski, Efficient rational approximation of optical response functions with the AAA algorithm, Laser Photon. Rev. **18**, 2400584 (2024).

[23] J. Ren, S. Franke, and S. Hughes, Connecting classical and quantum mode theories for coupled lossy cavity resonators using quasinormal modes, ACS Photonics **9**, 138 (2022).

[24] M. K. Dezfouli and S. Hughes, Quantum optics model of surface-enhanced Raman spectroscopy for arbitrarily shaped plasmonic resonators, ACS Photonics **4**, 1245 (2017).

[25] S. Both and T. Weiss, Resonant states and their role in nanophotonics, Semicond. Sci. Technol. **37**, 013002 (2021).

[26] M. I. Abdelrahman and B. Gralak, Completeness and divergence-free behavior of the quasi-normal modes using causality principle, OSA Continuum **1**, 340 (2018).

[27] E. A. Muljarov and T. Weiss, Resonant-state expansion for open optical systems: Generalization to magnetic, chiral, and bi-anisotropic materials, Opt. Lett. **43**, 1978 (2018).

[28] P. Lalanne, W. Yan, K. Vynck, C. Sauvan, and J.-P. Hugonin, Light interaction with photonic and plasmonic resonances, Laser Photon. Rev. **12**, 1700113 (2018).

[29] L. Gross, Norm invariance of mass-zero equations under the conformal group, J. Math. Phys. **5**, 687 (1964).

[30] Y. B. Zel'dovich, The number of quanta as an invariant of classical electromagnetic field, Proc. USSR Acad. Sci. **163**, 1359 (1965).

[31] I. Bialynicki-Birula and Z. Bialynicka-Birula, *Quantum Electrodynamics* (Pergamon, Oxford, 1975).

[32] H. Bateman, The transformation of the electrodynamical equations, Proc. Lond. Math. Soc. **s2-8**, 223 (1910).

[33] I. Fernandez-Corbaton and M. Vavilin, A scalar product for computing fundamental quantities in matter, Symmetry **15**, 1839 (2023).

[34] I. Fernandez-Corbaton, An algebraic approach to light–matter interactions, Adv. Phys. Res. **4**, 2400088 (2024).

[35] U. Hohenester and A. Trügler, MNPBEM – A Matlab toolbox for the simulation of plasmonic nanoparticles, Comput. Phys. Commun. **183**, 370 (2012).

[36] U. Hohenester, N. Reichelt, and G. Unger, Nanophotonic resonance modes with the NANOBEM toolbox, Comput. Phys. Commun. **276**, 108337 (2022).

[37] S. Woska, L. Rebholz, P. Rietz, and H. Kalt, Intrinsic mode coupling in mirror-symmetric whispering gallery resonators, Opt. Express **30**, 32847 (2022).

[38] G. B. Arfken, H.-J. Weber, and F. E. Harris, *Mathematical Methods for Physicists: A Comprehensive Guide* (Academic Press, New York, 2012).

[39] M. Vavilin, C. Rockstuhl, and I. Fernandez-Corbaton, Electromagnetic scalar product in spatially bounded domains, Phys. Rev. A **109**, 043506 (2024).

[40] R. Kress, in *Scattering*, edited by E. Pike and P. C. Sabatier (Academic Press, London, 2001).

[41] A. Lakhtakia, *Beltrami Fields in Chiral Media* (World Scientific, Singapore, 1994).

[42] I. Bialynicki-Birula, *V Photon Wave Function* (Elsevier, New York, 1996), p. 245.

[43] G. Kaiser, *A friendly Guide to Wavelets* (Springer Science & Business Media, Berlin, 2010).

[44] JCMwave GmbH Berlin, JCMsuite Documentation (2019), https://www.jcmwave.com/docs/ParameterReference/.

[45] Lumerical Inc, MODE: Waveguide Simulator (2024), https://www.lumerical.com/.

[46] COMSOL Inc, COMSOL multiphysics reference manual, version 5.3 (2024), www.comsol.com.

[47] K. Hiremath, M. Hammer, R. Stoffer, L. Prkna, and J. Čtyrokỳ, Analytic approach to dielectric optical bent slab waveguides, Opt. Quantum Electron. **37**, 37 (2005).

[48] K. Hiremath, R. Stoffer, and M. Hammer, Modeling of circular integrated optical microresonators by 2-D frequency domain coupled mode theory, Opt. Commun. **257**, 277 (2006).

[49] M. Paszkiewicz, M. Sukhova, W. Dörfler, and C. Rockstuhl, Approximation method for fast calculation of transmission in multi-mode waveguides, J. Opt. Soc. Am. A **41**, 174 (2024).